

H₂CO and CH₃OH abundances in the envelopes around low-mass protostars

J.K. Jørgensen¹*, F.L. Schöier², and E.F. van Dishoeck¹

¹ Leiden Observatory, P.O. Box 9513, NL-2300 RA Leiden, The Netherlands

² Stockholm Observatory, AlbaNova, SE-106 91 Stockholm, Sweden

Received ;date; / Accepted ;date;

Abstract. This paper presents the third in a series of single-dish studies of molecular abundances in the envelopes around a large sample of 18 low-mass pre- and protostellar objects. It focuses on typical grain mantle products and organic molecules, including H₂CO, CH₃OH and CH₃CN. With a few exceptions, all H₂CO lines can be fit by constant abundances of 7×10^{-11} – 8×10^{-9} throughout the envelopes if ortho- and para lines are considered independently. The current observational dataset does not require a large H₂CO abundance enhancement in the inner warm regions, but this can also not be ruled out. Through comparison of the H₂CO abundances of the entire sample, the H₂CO ortho-para ratio is constrained to be 1.6 ± 0.3 consistent with thermalization on grains at temperatures of 10–15 K. The H₂CO abundances can be related to the empirical chemical network established on the basis of our previously reported survey of other species and is found to be closely correlated with that of the nitrogen-bearing molecules. These correlations reflect the freeze-out of molecules at low temperatures and high densities, with the constant H₂CO abundance being a measure of the size of the freeze-out zone. An improved fit to the data is obtained with a ‘drop’ abundance structure in which the abundance is typically a few $\times 10^{-10}$ when the temperature is lower than the evaporation temperature and the density high enough so that the timescale for depletion is less than the lifetime of the core. The location of the freeze-out zone is constrained from CO observations. Outside the freeze-out zone, the H₂CO abundance is typically a few $\times 10^{-9}$ – 10^{-8} . The observations show that the CH₃OH lines are significantly broader than the H₂CO lines, indicating that they probe kinematically distinct regions. CH₃OH is moreover only detected toward a handful of sources and CH₃CN toward only one, NGC 1333-IRAS2. For NGC 1333-IRAS2, CH₃OH and CH₃CN abundance enhancements of two-three orders of magnitude at temperatures higher than 90 K are derived. In contrast, the NGC 1333-IRAS4A and IRAS4B CH₃OH data are fitted with a constant abundance and an abundance enhancement at a lower temperature of 30 K, respectively. This is consistent with a scenario where CH₃OH probes the action of compact outflows on the envelopes, which is further supported by comparison to high frequency, high excitation CS $J = 10-9$ and HDO line profiles which uniquely probe warm, dense gas. The extent to which the outflow dominates the abundance enhancements compared with the passively heated inner envelope depends on the filling factors of the two components in the observing beam.

Key words. stars: formation, ISM: molecules, ISM: abundances, radiative transfer, astrochemistry

1. Introduction

The chemistry of organic molecules in the envelopes around low-mass protostars is likely to reflect directly in the molecular composition of their circumstellar disks and eventual protoplanetary systems. A number of competing mechanisms are important in regulating the chemistry in these early deeply embedded stages: the heating of protostellar cores due to central, newly formed stars results in evaporation of ices in the innermost regions whereas shocks related to the ubiquitous outflows may liberate ice mantles and trigger similar effects but on larger scales. These mechanisms have been suggested to be

the cause of enhancements of, e.g., H₂O, H₂CO and CH₃OH on small scales in the envelopes (e.g., Ceccarelli et al., 1998, 2000; Schöier et al., 2002, 2004). This paper, the third in a series, presents an analysis of, in particular, H₂CO and CH₃OH abundances in the sample of 18 protostars studied in a wide range of other molecules by Jørgensen et al. (2002, 2004c). Those papers discussed observations of molecular species predominantly probing the outer cold envelopes around these objects. It was found that freeze-out at low temperatures and high densities dominates the chemistry and that, in particular, the freeze-out of CO is reflected in the abundances of a number of related species at large distances from the central protostar. This paper complements the study of H₂CO and CH₃OH in a subset of objects by Maret et al. (2004, 2005). Both species are typical grain-mantle products observed in interstellar ices. To fully appreciate their chemistry it is important to compare

Send offprint requests to: Jes K. Jørgensen

* Present address: Harvard-Smithsonian Center for Astrophysics, 60 Garden Street MS42, Cambridge, MA 02138, USA

Correspondence to: jjorgensen@cfa.harvard.edu

their abundances with the more general chemical network. For example, high resolution observations of Schöier et al. (2004) indicate that the H₂CO abundance structures may be related to the “drop abundance” structures inferred from CO observations (Jørgensen et al., 2005). In these drop abundance profiles, freeze-out occurs in a limited region of the envelope where the temperature is low enough to prevent immediate desorption (typically < 40 K) but the density still high enough that the timescale for depletion is less than the lifetime of the core (see also Fig. 10 of Schöier et al. (2004)).

The class 0 protostar, IRAS 16293-2422, has long been the template for astrochemistry studies of deeply embedded low-mass protostars due to its rich spectrum (Blake et al., 1994; van Dishoeck et al., 1995). IRAS 16293-2422 has a central warm and dense gas core where ices evaporate. Recently, Cazaux et al. (2003) have shown the existence of a large number of complex organic species in IRAS 16293-2422, further underscoring the rich chemistry of this particular source. It remains an interesting question whether this simply reflect “first generation” evaporation of organic molecules at high temperatures or whether the timescales are indeed long enough that a “second generation” hot core chemistry can evolve in the innermost regions of these envelopes (see, e.g., discussion in Schöier et al., 2002).

To put the IRAS 16293-2422 results in context, it is important to expand the sample of well-studied protostars. Jørgensen et al. (2004c) presented a survey of molecular species probing the cold outer component of protostellar objects with different envelope masses, i.e., both “class 0” and “class I” objects. Although large variations in abundances occur within the sample, it was found that IRAS 16293-2422 is in no way unique. The same objects were observed in transitions of H₂CO and CH₃OH at the JCMT. Maret et al. (2004) presented the H₂CO observations, together with observations from the IRAM 30 m telescope, for a subset of exclusively class 0 objects. They reported the existence (or possibility) of H₂CO abundance jumps (i.e., abundance enhancements in the innermost regions of the envelopes at $T > 90$ K where all ices evaporate), in some cases up to four orders of magnitude. However, Schöier et al. (2004) showed through high angular resolution data of IRAS 16293-2422 and L1448-C, that the exact abundance structure of the outer envelopes may severely affect the interpretation of the innermost envelope. For these low luminosity sources the warm inner regions have diameters < 100 AU (< 0.5”), i.e., are significantly diluted for single-dish observations with typical beam sizes of 15 – 30”.

Buckle & Fuller (2002) studied the low excitation ($3_K - 2_K$) lines of CH₃OH toward a large sample of class 0 and I objects. They found that a large fraction of the sources, predominantly the class 0 objects, show lines with two velocity components with CH₃OH being enhanced by up to two orders of magnitude. Buckle & Fuller suggested that the broad component is due to outflow generated shocks heating the envelope material and thus liberating the grain mantles. Similar effects are also observed in several well-studied “isolated” outflows well separated from the protostars themselves (Bachiller et al., 1995; Bachiller & Pérez Gutiérrez, 1997; Jørgensen et al., 2004a). These and other studies illustrate that for CH₃OH, a big is-

sue may be whether the abundance enhancements derived from single-dish observations toward protostellar cores are related to passive heating or the action of outflows.

This paper expands the work of Maret et al. (2004, 2005) through observations and modeling of H₂CO, CH₃OH and CH₃CN emission for the entire sample of pre- and protostellar cores studied by Jørgensen et al. (2002, 2004c), adopting the same physical models and approach as in these papers. In addition, we present high excitation CS $J = 10-9$ and HDO observations which uniquely probe the dense and warm gas in the envelope. Sect. 2 presents the observations forming the basis of this study. Sect. 3 describes the model approach, highlighting the similarities and differences with the work of Maret et al. (2004). Sect. 4 discusses the results, focusing on the distinction between passively heated and shock processed material. Based on this study, it is discussed which objects are good candidates for further studies of low-mass protostars with a “hot core” chemistry.

2. Observations

2.1. General issues

The sample of 18 pre- and protostars presented by Jørgensen et al. (2002) was observed in a wide range of lines at the James Clerk Maxwell Telescope from 2001 through 2003. The observations of other species besides H₂CO, CH₃OH and CH₃CN are discussed by Jørgensen et al. (2004c). Maret et al. (2004, 2005) reported H₂CO and CH₃OH observations, respectively, toward the sources with the most massive envelopes - and hence strongest lines - in the sample, which are also included in this paper. The following sections discuss the observations of each of these species in detail. All lines were observed and reduced in a standard way: pointing was checked regularly at the telescope and typically found to be accurate to within a few arcseconds. Calibration was checked by observations of line standards and found to be accurate to within 20%. The A3 and B3 receivers at 1.3 and 0.8 mm were used: the telescope beam sizes are typically 21” and 14” at these frequencies. The velocity resolution ranged from 0.13 to 0.55 km s⁻¹ for the different line settings. Low order polynomials were subtracted and the spectra were brought onto the T_{MB} scale through division by the main beam efficiencies, η_{MB} . Values of η_{MB} of 0.69 and 0.63 were adopted for the 230 GHz observations with receiver A3 and the 345 GHz observations with receiver B3, respectively.

Most of the observed lines are remarkably symmetric and for these lines, a single Gaussian could be fitted. The only exceptions are a few of the lowest excitation lines, which are integrated over ± 2 km s⁻¹ from the systemic velocity. This velocity interval covers the emission from the quiescent envelope material as judged from the optically thin Gaussian lines. The line intensities for all species are given in Tables 1–4. The corresponding line widths are given in Tables A.1–A.2 in the appendix. For the non-detections, 3σ upper limits are reported with $\sigma = 1.2 \sqrt{\delta v \Delta_0 v} T_{\text{RMS}}$ where δv is the velocity resolution, $\Delta_0 v$ the expected line width to zero intensity (assumed to be

4 km s⁻¹), T_{RMS} the RMS noise level for the given resolution and the factor 1.2 introducing the 20% calibration uncertainty.

In addition to these observations, the high frequency RxW receiver was used to observe CS $J = 10 - 9$ at 489.751 GHz for four sources (L1448-C, NGC 1333-IRAS2, -IRAS4A and -IRAS4B) over two nights in November 2002. Special care was taken with the calibration: comparison with nearby spectral standards was found to vary by < 20% over these two nights, during which the sky opacity was $\lesssim 0.05$ at 225 GHz and the elevation of the sources higher than $\approx 50^\circ$. Still, high system temperatures of up to ~ 5000 K were found and this, together with the pointing uncertainties of a few arcseconds of the JCMT (compared to a beam size of $10''$), may cause the absolute calibration to be somewhat uncertain for these observations. The CS 10–9 lines were detected toward NGC 1333-IRAS4A and IRAS4B but not L1448-C and NGC 1333-IRAS2. The implications of these observations are discussed further in Sect. 4.2.

2.2. H₂CO

In addition to the observations presented by Maret et al. (2004), H₂CO emission from the ortho $5_{15} - 4_{14}$ line at 351.768 GHz and the para $5_{05} - 4_{04}$ line at 362.736 GHz was observed for all sources. Furthermore JCMT archival data exist for the para $3_{03} - 2_{02}$ and $3_{22} - 2_{21}$ lines at 218.222 and 218.475 GHz for most sources and these observations were included for those sources not observed at the IRAM 30m by Maret et al. (2004). Table 1 lists the line intensities for all sources. The typical line widths of the H₂CO lines are 1–2 km s⁻¹ (FWHM). For the prestellar cores, L1544 and L1689B, intensities of $J = 2 - 1$ and $3 - 2$ lines from IRAM 30 m observations by Bacmann et al. (2003) were included in the modeling.

2.3. CH₃OH

The CH₃OH $7_K - 6_K$ observations of the sources in NGC 1333 are presented in Maret et al. (2005). In addition, the $5_K - 4_K$ band at 241 GHz was observed for the NGC 1333 sources. The line intensities from the $5_K - 4_K$ band data are given in Table 2. Table 3 lists the CH₃OH observations for the remaining sources. Only the NGC 1333 sources have detections for a large number of CH₃OH lines. Besides these, only L723, L1448-C and VLA 1623 show detections in the $7_K - 6_K$ band and only of 1–2 lines each. The HDO $2_{11} - 2_{12}$ transition at 241.5616 GHz was covered in the CH₃OH $5_K - 4_K$ setting, but was only detected toward NGC 1333-IRAS2.

As for H₂CO, the CH₃OH lines can be divided into two forms, A- and E-type, depending on the rotation of the methyl CH₃-group with respect to the OH group. Some systematics, which may give clues to the origin of the CH₃OH emission, can be directly inferred from these results. For example, NGC 1333-IRAS2 shows the highest excitation lines for both the A and E-type for the $5_K - 4_K$ and $7_K - 6_K$ transitions compared to NGC 1333-IRAS4A and -IRAS4B. Still, the lowest excitation lines toward NGC 1333-IRAS2 are weaker than those toward the NGC 1333-IRAS4 sources: barring pure exci-

Table 1. Integrated H₂CO line intensities ($\int T_{\text{MB}} dv$ [K km s⁻¹]).

	p-H ₂ CO		o-H ₂ CO	
	$3_{03} - 2_{02}^b$	$3_{22} - 2_{21}^b$	$5_{05} - 4_{04}$	$5_{15} - 4_{14}$
L1448-I2	<0.9	1.2
L1448-C ^a	3.4	0.4	1.3	1.0
N1333-I2 ^a	4.9	1.0	1.8	1.6
N1333-I4A ^a	9.3	2.2	2.9	5.5
N1333-I4B ^a	9.6	4.7	5.9	7.5
L1527 ^a	3.0	0.2	0.4	1.0
VLA1623 ^a	5.0	...	1.2	0.9
L483	2.3	< 0.2	1.2	1.3
L723	1.1 ^c	< 0.1 ^c	1.1	2.0
L1157 ^a	1.1	< 0.3	0.5	1.2
CB244	0.9	< 0.4	0.6	1.4
L1489	<0.3	<0.3	<0.4	0.7
TMR1	0.6	<0.1	<0.3	0.4
L1544	0.3 ^d	...	<0.5	<0.4
L1689B	1.7 ^d	1.0 ^d	<0.3	<0.4

^aObservations previously reported by Maret et al. (2004). For some of these sources additional o-H₂CO $2_{12} - 1_{11}$ and $4_{14} - 3_{13}$, p-H₂CO $5_{24} - 4_{23}$ and o-H¹³CO observations and limits were reported by Maret et al. (2004). ^b $3_{03} - 2_{02}$ and $3_{22} - 2_{21}$ line intensities from Maret et al. (2004) are from IRAM 30 m observations. ^cFrom SEST (HPBW=24'') observations. ^dIRAM 30 m observations from Bacmann et al. (2003): for these two pre-stellar cores o-H₂CO $2_{12} - 1_{11}$ observations were also reported by Bacmann et al. and included in the modeling.

tation/opacity effects, this could be interpreted as a warmer interior, possibly with higher abundances in NGC 1333-IRAS2. In particular, since the sources otherwise have relatively similar physical structures these differences suggest that one or more sources will show chemical gradients. Furthermore the CH₃OH lines are significantly broader with line widths of 4–6 km s⁻¹ (FWHM) compared to 1–2 km s⁻¹ found for H₂CO and the other species in Jørgensen et al. (2002, 2004c).

2.4. CH₃CN

CH₃CN $14_K - 13_K$ was observed at 257.5 GHz for the NGC 1333 sources with 2 hours integration time per source, reaching RMS levels of 0.02 K (T_{MB}) in 0.36 km s⁻¹ channels. At these levels the $K = 0, \dots, 3$ components are detected for NGC 1333-IRAS2, as shown in Fig. 1. Since NGC 1333-IRAS2 typically shows weaker lines for other molecules than the two NGC 1333-IRAS4 sources (see, e.g., Jørgensen et al., 2004c), this suggests that CH₃CN may probe a different chemical regime (together with the CH₃OH lines) than the bulk, cold envelope in this source. Recently Bottinelli et al. (2004) reported detections at the 40-70 mK ($T_{\text{MB}}(\text{peak})$) of the CH₃CN $14_K - 13_K$ components from IRAM 30 m observations toward NGC 1333-IRAS4A. These are consistent with our upper limits taking into account the smaller beam size of the IRAM 30 m telescope.

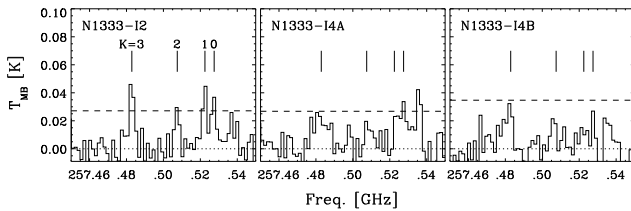
Table 2. CH₃OH 5_K–4_K line intensities ($\int T_{\text{MB}} dv$ [K km s⁻¹]) for sources in NGC 1333.

Line	Frequency	IRAS2	IRAS4A	IRAS4B
5 _K –4 _K band; E-type				
+0E	241.7002	0.41	2.9	2.1
–1E	.7672	0.86	7.8	4.6
–4E	.8132	0.17	<0.06	<0.06
+4E	.8296	0.16	<0.06	<0.06
+3E	.8430	0.30	0.48	0.55 †
–3E	.8523	0.17	<0.06	<0.06
+1E	.8790	0.33	1.3	1.3
±2E	.9044	0.45	2.7	2.3
5 _K –4 _K band; A-type				
+0A	241.7914	1.1	8.9	5.3
±4A	.8065	0.18	<0.06	< 0.06
±3A	.8329	0.33	0.64	0.53
–2A	.8430	0.30	0.48	0.55 †
+2A	.8877	0.23	0.49	0.50

“†”The 5–4 +3E and –2A lines are blended at 241.8430 GHz and have therefore (although observed) been excluded from the modeling. The quoted intensity refers to the total intensity of both lines.

Table 3. CH₃OH line intensities ($\int T_{\text{MB}} dv$ [K km s⁻¹]) and limits for sources not in NGC 1333.

	7–6	
	–1E	0A+
L1448-I2	< 0.09	
L1448-C	0.254	0.415
L1527	< 0.12	
VLA1623	0.063	0.060
L483	< 0.18	
L723	< 0.06	0.373
L1157	< 0.18	
CB244	< 0.12	
L1489	< 0.09	
TMR1	< 0.09	

**Fig. 1.** CH₃CN 14_K–13_K line observations at 257.5 GHz of the NGC 1333 sources. The vertical lines indicate the expected locations of the $K = 0, 1, 2, 3$ lines. The dashed line indicates the 3σ detection limit.

3. Modeling

To model the chemical abundances the approach described in Jørgensen et al. (2002, 2004c) and Schöier et al. (2002), and utilized for the entire sample of sources and molecules, was

Table 4. CH₃CN and CH₃OCH₃ line intensities ($\int T_{\text{MB}} dv$ [K km s⁻¹]) and 3σ upper limits for the sources in NGC 1333.

Line	Frequency	IRAS2	IRAS4A	IRAS4B
CH ₃ CN				
14 ₃ –13 ₃	257.4828	0.20	<0.09 ^a	<0.1
14 ₂ –13 ₂	257.5076	0.10	–	–
14 ₁ –13 ₁	257.5224	0.17	–	–
14 ₀ –13 ₀	257.5274	0.15	–	–
CH ₃ OCH ₃				
13 _{1,13} –12 _{0,12}	241.9468	<0.08	<0.1	<0.1

^aBottinelli et al. (2004) report detection of the 14_K–13_K lines at the 40–70 mK level from IRAM 30m observations toward NGC 1333-IRAS4A.

adopted. Each species was modeled with the envelope physical structure from Jørgensen et al. (2002) derived from dust radiative transfer modeling of their submillimeter (SCUBA) continuum emission and SEDs. The line radiative transfer was then performed using the code of Schöier et al. (2002) constraining the average molecular abundances. This code was benchmarked to high accuracy against a large number of other line radiative transfer codes for a number of test problems by van Zadelhoff et al. (2002) and found to agree within the Monte Carlo noise.

A number of different trial abundance profiles are considered besides profiles with a constant abundance, X_0 , of a given molecule at all radii (see also Fig. 10 of Schöier et al. (2004)). In “jump” profiles the abundance increase from X_0 to X_j at a given temperature in the envelope, e.g., simulating ice mantle evaporation. Likewise “anti-jump” profiles have a decrease in abundance in the inner region. Finally, in “drop” profiles the abundance X_0 is high (comparable to the undepleted abundance expected in a warm molecular cloud without significant freeze-out), in the inner and outermost regions of the envelope. At radii where the temperature is lower than a molecule-specific desorption temperature T_{ev} and the density higher than the density n_{de} where the timescale for freeze-out is lower than the lifetime of the core, the abundance decreases to X_D .

For H₂CO the collisional rate coefficients used in Schöier et al. (2002) were adopted. As described by Maret et al. (2004), ortho H₂¹³CO lines are detected for the three sources in NGC 1333. The corresponding abundances were likewise calculated and taken into account in subsequent discussions. For CH₃OH, new collisional rate coefficients by Pottage et al. (2004) were used. For CH₃CN LTE excitation was assumed. The molecular data files are taken from the *Leiden Atomic and Molecular Database* (Schöier et al., 2005) and are publically available¹. Each of the ortho- and para H₂CO and the A- and E-type CH₃OH are treated as separate molecules, which is possible since radiative transitions between the different species are ruled out. In the first iteration, the abundances are kept constant throughout the envelope and the results from the best fits are given in Tables 5–7 below.

¹ <http://www.strw.leidenuniv.nl/~moldata>

Table 5. Inferred abundances for o-H₂CO, p-H₂CO and o-H₂¹³CO, reduced χ^2 and number of lines where applicable.

Source	M_{env} M_{\odot}	o-H ₂ CO			p-H ₂ CO		
		Abundance	χ_{red}^2	n_{lines}	Abundance	χ_{red}^2	n_{lines}
Class 0 objects ($M_{\text{env}} > 0.5M_{\odot}$)							
L1448-I2	1.5	3.0×10^{-10}	...	1	$< 1.8 \times 10^{-10}$...	(1)
L1448-C	0.93	8.9×10^{-10}	1.2	3	6.8×10^{-10}	1.0	4
N1333-I2	1.7	4.3×10^{-10}	0.63	3	3.9×10^{-10}	1.3	4
N1333-I4A	2.3	3.4×10^{-10}	0.59	3	2.3×10^{-10}	3.1	4
N1333-I4B	2.0	8.7×10^{-10}	6.2	3	4.1×10^{-9}	0.96	4
L1527	0.91	8.4×10^{-10}	7.7	3	8.4×10^{-10}	0.44	3
VLA1623	0.22	7.7×10^{-10}	0.34	3	1.3×10^{-9}	0.061	2
L483	4.4	6.3×10^{-10}	...	1	3.3×10^{-10}	6.7	2
L723	0.62	3.1×10^{-9}	...	1	9.6×10^{-10}	2.6	2
L1157	1.6	9.2×10^{-11}	3.9	3	3.6×10^{-11}	2.1	2
Class I objects ($M_{\text{env}} < 0.5M_{\odot}$)							
CB244	0.28	5.3×10^{-9}	...	1	6.9×10^{-10}	10.9	2
L1489	0.097	2.7×10^{-9}	...	1	$< 1.4 \times 10^{-9}$...	(1)
TMR1	0.12	5.0×10^{-9}	...	1	3.4×10^{-9}	...	1+(1)
Pre-stellar cores							
L1544 ^a	2.5	4.0×10^{-11}	...	1	3.0×10^{-11}	...	1
L1689B ^a	2.5	2.0×10^{-10}	8.4	2+(1)	1.2×10^{-10}	0.6	2
o-H ₂ ¹³ CO							
N1333-I2	1.7	3.0×10^{-11}	3.3	2			
N1333-I4A	2.3	5.2×10^{-12}	2.5	3			
N1333-I4B	2.0	8.0×10^{-11}	...	1			

^aQuoted value based on line intensities reported by Bacmann et al. (2003). Upper limits from JCMT lines only are one to two orders of magnitude larger.

Table 7. Inferred abundances and reduced χ^2 from models of CH₃CN toward IRAS2.

Source	Abundance	χ_{red}^2	n_{lines}
CH ₃ CN			
N1333-I2	8.3×10^{-11}	8.5	4
	7×10^{-9a}	1.4	4

^aAbundance in inner ($T > 90$ K) region. 3σ upper limit on the abundance in the outer envelope of 2×10^{-11} .

3.1. H₂CO

For most sources the H₂CO line intensities are well-fit with constant abundance models for each of the p-H₂CO and o-H₂CO species. For a few sources, one of these two has a χ_{red}^2 higher than 3 (o-H₂CO: NGC 1333-IRAS4B, L1527, L1157 and L1689B; p-H₂CO: NGC 1333-IRAS4A, L483 and CB244). This is in contrast to Maret et al. (2004) who inferred large abundance jumps for the studied sources. As shown below this is due to a number of differences in the assumptions between the work of Maret et al. (2004) and this study, in particular the ortho-para ratio. Below we discuss some of these differences.

3.1.1. Velocity structure

Maret et al. (2004) assume a non-turbulent but infalling envelope, whereas our work assumes a constant turbulent broadening of 0.5–1 km s⁻¹ throughout the envelopes reproducing the observed line widths. The derived abundances do not depend on the velocity field if only optically thin lines are considered (Jørgensen et al., 2004c). For the constant abundances listed above, the observed lines have typical optical depths of 0.1–1. This constant width may not be an adequate description of emission originating from the innermost dense regions in the case of large abundance jumps, but in the context of an inside-out collapsing envelope, the outer envelope will naturally be characterized by the turbulent broadening. In class 0 objects typical inferred ages are $\sim 10^4$ years, which for typical values of the sound speed of 0.3–0.5 km s⁻¹ translate to infall radii of 500–1000 AU. Such sizes are unresolved by single-dish observations and even by medium-high resolution interferometer data. This implies that the infall radius encompasses the hot inner region, but that most of the mass in the envelope material is not infalling.

From line radiative transfer it is possible to make exact predictions for the line profiles, which can be compared to the observed spectra to constrain the velocity field. Fig. 2 compares the observed 5₀₅–4₀₄ and 5₁₅–4₁₄ spectra toward L1448-C with the modeled line profiles adopting the non-infalling but turbulent envelope model (with constant H₂CO abundance) from this

Table 6. Inferred abundances for CH₃OH, reduced χ^2 and number of lines where applicable.

Source	CH ₃ OH A-type			CH ₃ OH E-type		
	Abundance	χ^2_{red}	n_{lines}	Abundance	χ^2_{red}	n_{lines}
Class 0 objects ($M_{\text{env}} > 0.5 M_{\odot}$)						
L1448-I2	$<1.1 \times 10^{-10}$...	(1)	$<1.4 \times 10^{-10}$...	(1)
L1448-C	1.3×10^{-9a}	...	1	1.0×10^{-9a}	...	1
N1333-I2	1.4×10^{-9a}	20.4	8	1.3×10^{-9a}	18.4	13
N1333-I4A	2.9×10^{-9a}	4.5	7	2.5×10^{-9a}	3.1	7
N1333-I4B	3.5×10^{-8a}	11.4	7	9.1×10^{-9a}	9.6	7
L1527	$<5.5 \times 10^{-10}$...	(1)	$<6.8 \times 10^{-10}$...	(1)
VLA1623	2.5×10^{-10}	...	1	3.4×10^{-10}	...	1
L483	$<2.2 \times 10^{-10}$...	(1)	$<2.7 \times 10^{-10}$...	(1)
L723	1.8×10^{-9}	...	1	$<3.6 \times 10^{-10}$...	(1)
L1157	$<2.7 \times 10^{-10a}$...	(1)	$<3.4 \times 10^{-10a}$...	(1)
Class I objects ($M_{\text{env}} < 0.5 M_{\odot}$)						
CB244	$<1.0 \times 10^{-9}$...	(1)	$<1.3 \times 10^{-9}$...	(1)
L1489	$<9.9 \times 10^{-10}$...	(1)	$<1.2 \times 10^{-9}$...	(1)
TMR1	$<2.2 \times 10^{-9}$...	(1)	$<2.8 \times 10^{-9}$...	(1)

^aSee also Maret et al. (2005).

paper and the non-turbulent, infalling model (with abundance jump) from Maret et al. (2004). Considering only the higher excitation H₂CO $J = 5-4$ lines should limit confusion from the surrounding material. It is seen that the “turbulent” envelope model clearly provides the closest match to the observed line profile, whereas the non-turbulent, infalling model provides too much broadening. It is interesting to note that the same turbulent broadening which is used to fit low-excitation CO isotopic lines from the cold, outer envelope (Jørgensen et al., 2002) works well in also explaining the observed H₂CO line widths. In the context of, e.g., an inside-out collapsing envelope as in Shu (1977) this suggests that the infalling region of the envelope is small and that even the relatively high excitation H₂CO lines studied in this paper are still predominantly sensitive to the outer envelope. It is worth re-emphasizing that both turbulent and non-turbulent/infalling models give a good constant abundance fit when the ortho and para lines are treated independently and that abundance jumps are in general not required for the studied sources, other than in the context of a “drop model” (see Sect. 3.1.3). Naturally a combination of turbulent broadening and systematic motions (e.g., infall) most likely applies to the studied envelopes and a fully self-consistent model explaining also emission of optically thick lines would have to take these into account. Observations of optically thick transitions of, e.g., HCO⁺ could be used to constrain such models, but this is beyond the scope of the present study.

3.1.2. H₂CO ortho-para ratio

A second difference with Maret et al. (2004) is the assumption of a fixed ortho/para ratio. Since para and ortho H₂CO can be considered to be separate molecules, their abundances can be determined independently. Fig. 3 compares the abundances for the two species. A very close correlation exists (Pearson cor-

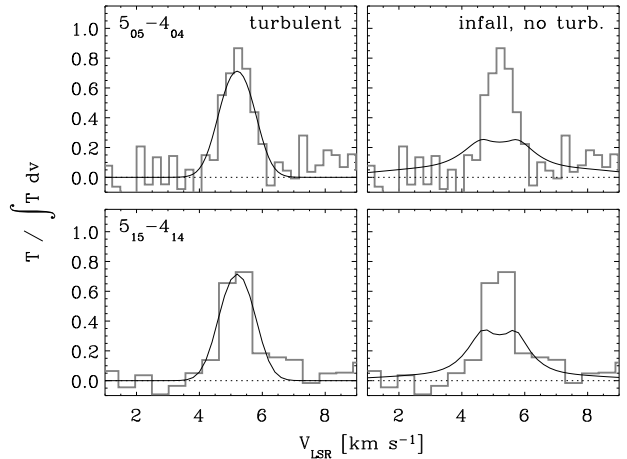


Fig. 2. Spectra and modeled line profiles of the $5_{05} - 4_{04}$ (para) and $5_{15} - 4_{14}$ (ortho) H₂CO lines (upper and lower panels, respectively) toward L1448-C in a pure turbulent, constant abundance envelope (this paper; left) and in a non-turbulent envelope with an abundance jump infalling toward a $0.5 M_{\odot}$ central object (Maret et al. (2004); right). The spectra have all been normalized by division with the total integrated line intensity to bring out more clearly the comparison between the actual line shapes.

relation coefficient of 0.9; see also Sect. 3.1.3), which can be fitted by an ortho-para ratio of 1.6 ± 0.3 . The very tight correlation indicates that both species probe the same region of the envelope and that their abundance ratios are established under similar conditions in all sources.

Maret et al. (2004) assumed an ortho-para ratio of 3 to combine o-H₂CO and p-H₂CO line observations to constrain the abundance structure. Whereas this gives in principle fewer free

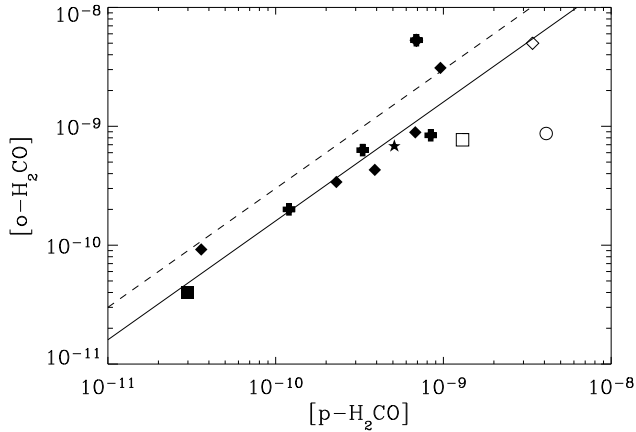


Fig. 3. Comparison between the abundances of the p-H₂CO and o-H₂CO species. The class 0 objects are indicated by filled diamonds, the class I objects by open diamonds and the pre-stellar cores by filled squares. The class 0 objects VLA1623 and IRAS 16293-2422 have been singled out by an open square and star, respectively. Sources with poor fits ($\chi_{\text{red}}^2 \geq 5$) to either the p-H₂CO or o-H₂CO species are indicated by black crosses. Of these N1333-I4B has further been singled-out with the open circle. The statistical uncertainties from the fits including calibration uncertainties are 10–20%, i.e., the error bars are of similar size as the plot symbols. The solid line indicates the best fit linear correlation between the two sets of abundances (excluding the poorly fit sources), corresponding to an ortho-para ratio of 1.6:1. The dashed line indicates the relation for an ortho-para ratio of 3:1.

parameters in the modeling, one should be careful when interpreting the results. This is clearly illustrated in Fig. 4 where constraints on the total H₂CO abundance from ortho and para lines for L1448-C are shown. It can be seen that the overlapping confidence levels depend critically on the adopted ortho-para ratio, with a high ortho-para ratio driving an increased abundance jump in the inner envelope up to 4 orders of magnitude. For both species a constant abundance model provides a good fit to the observed lines and the combination of the two suggests an ortho-para ratio of 1.6, in agreement with the conclusion above. Fig. 5 compares the modeled and observed line intensities for L1448-C as functions of energy level of the observed H₂CO transitions. No systematics are seen (for example, transitions from higher levels are not systematically underestimated in the models) and almost all observed intensities are well reproduced within the observational uncertainty. In general, it is difficult to constrain the ortho-para ratio for a specific source because of the intrinsic uncertainty in the observations and modeling, including varying ortho-para ratios with position and varying optical depth (Schöier et al., 2002). The strength of our analysis is that the ratio is based on a large sample of sources, statistically reducing some of these uncertainties.

The ortho-para ratio itself contains interesting information about the H₂CO formation, as discussed by Kahane et al. (1984). At high temperatures the ortho-para ratio approaches the relative statistical weights of 3:1, but thermalization at

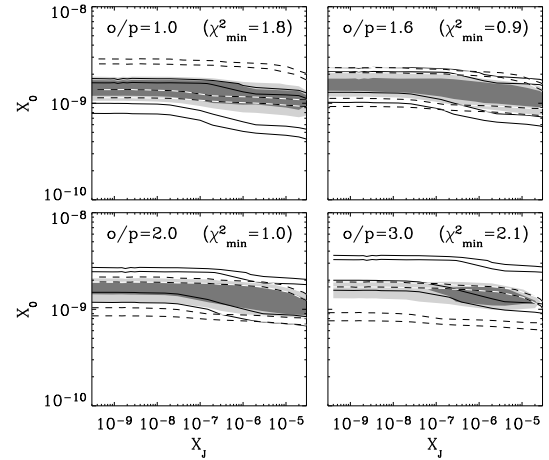


Fig. 4. Constraints on the H₂CO abundances in the inner ($T > 90$ K) and outer ($T < 90$ K) envelope (X_J and X_0 , respectively) and effect of adopted ortho-para ratio for L1448-C. A non-turbulent, free-falling envelope has been adopted as in Maret et al. (2004). The solid line contours indicate the 2 and 4 σ confidence levels for ortho-H₂CO, whereas the dashed line contours indicate the corresponding confidence levels for p-H₂CO. The grey scale contours indicate similar confidence levels for the H₂CO abundance combining the constraints from the two datasets and assuming the ortho-para ratios of 1.0, 1.6, 2.0 and 3.0, respectively, as indicated in the top of each panel.

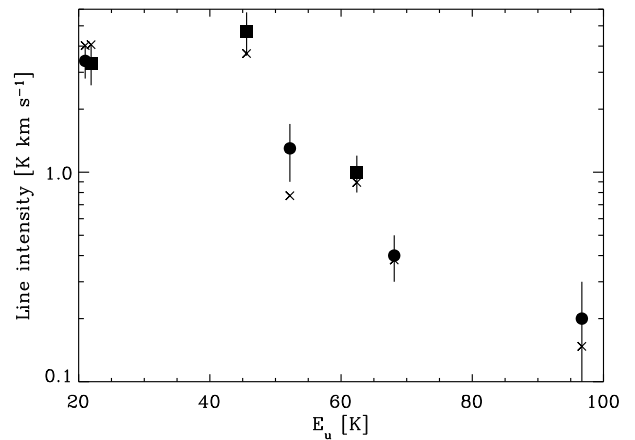


Fig. 5. Comparison between observed and modeled line intensities as function of the energy of the upper level for each H₂CO transition toward L1448-C. The observed intensities of the para lines are indicated by the circles, the intensities of ortho lines by the squares and the modeled intensities by the crosses.

lower temperatures ($T \sim 10 - 15$ K) makes the two abundances closer to equal. As argued by Kahane et al., gas-phase thermalization is improbable: the life-times of the established ortho-para species are significantly longer than, e.g., the time it takes to destroy a given H₂CO molecule through reactions with molecular ions. Kahane et al. furthermore find that chemical reactions lead to ortho-para ratios of 3–5. In contrast, H₂CO

Table 8. Pearson correlation coefficients between abundances found in this paper and abundances from Jørgensen et al. (2004c).

	p-H ₂ CO	o-H ₂ CO
CO	0.63	0.70
HCO ⁺	0.46	0.76
CS	0.42	0.60
SO	0.13	0.05
HCN	0.72	0.63
HNC	0.57	0.74
CN	0.57	0.81
HC ₃ N	0.44	0.70
p-H ₂ CO	...	0.92
o-H ₂ CO	0.92	...

can be thermalized on dust grains and released subsequently. For grain temperatures of 10–15 K, an ortho-para ratio of 1.5 is in good agreement with the results from this paper. This is also what is found in typical dark clouds such as TMC1 and L134N, whereas warmer regions such as the Orion clouds show ortho-para ratios closer to the statistical 3:1 ratio (Kahane et al., 1984; Mangum & Wootten, 1993). The derived ortho-para ratio of 1.6 ± 0.3 for the sources in this sample therefore suggests that the observed H₂CO lines are predominantly sensitive to the outer cold envelope and that relative abundances of the ortho and para species are established there.

3.1.3. Comparison to other molecules and implications for abundance structures

To quantify the relations between the abundances of the observed molecular species, Jørgensen et al. (2004c) calculated Pearson correlation coefficients for each pair of abundances. The Pearson correlation coefficient, P , is a measure of how well a (x, y) data set is fit by a linear correlation compared to the spread of (x, y) points. Values of ± 1 indicate good correlations (with positive or negative slopes) whereas a value of 0 indicates no correlation. In our studies of other molecules, strong correlations ($|P| \geq 0.7$) were found between molecules for which relations were expected based on chemical considerations, for example between CO and HCO⁺ or between the sulfur-bearing species. To extend this discussion, correlation coefficients were calculated between the abundances found in this paper and those from Jørgensen et al. (2004c) (see Table 8).

An important conclusion is the apparent anti-correlation between the H₂CO abundances and envelope mass within the radius where the temperature drops to 10 K (Jørgensen et al., 2002) as shown in Fig. 6. This is also reflected in the correlations in Table 8 between H₂CO and molecules such as CO whose abundances decline with increasing mass (Jørgensen et al., 2002). Jørgensen et al. (2004c, 2005) suggested that this correlation is well explained with a drop-abundance profile, with the different H₂CO abundances reflecting the size of the region over which freeze-out occurs.

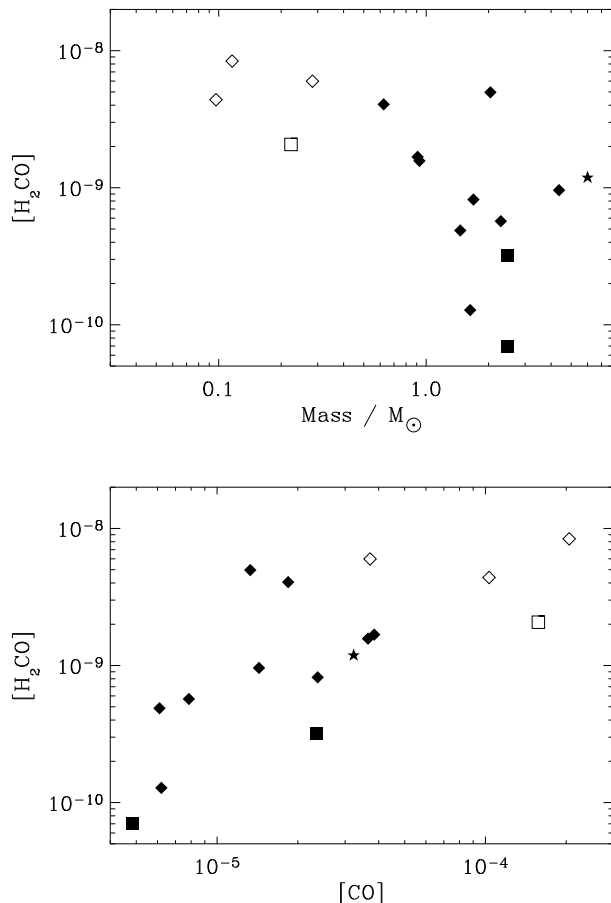


Fig. 6. Total H₂CO abundance vs. envelope mass (upper panel) and CO abundance (lower panel). The envelope mass refers to the mass within the radius where the temperature drops to 10 K as estimated from the dust radiative transfer models (see Jørgensen et al., 2002). For objects where only the abundance of one of the two H₂CO species has been constrained, an ortho-para ratio of 1.6 is assumed. As in Fig. 3 the class 0 objects are indicated by “♦”, the class I objects by “◇” and the pre-stellar cores by “■”. The class 0 objects VLA1623 and IRAS 16293-2422 have been singled out by “□” and “★”, respectively.

As an illustration, the drop abundance structure is tested for the H₂CO lines toward NGC 1333-IRAS4A. For the H₂CO lines we first constrain the depletion density, n_{de} , and desorption temperature, T_{ev} , from observations of the CO lines presented by Jørgensen et al. (2002). The CO data toward NGC 1333-IRAS4A are well-fitted with depletion by a factor of 50 in the region of the envelope where the density is higher than $6 \times 10^5 \text{ cm}^{-3}$ and temperature lower than 40 K. These constraints are used as input for the H₂CO chemical structure, so that only the overall and depleted abundances, (X_0 and X_D , respectively) are left as free parameters. The results of these fits are shown in Fig. 7: both ortho and para lines are consistent with an abundance drop of approximately an order of magnitude. The χ^2 confidence regions for the two H₂CO species agree at the 1σ level assuming an ortho-para ratio of 1.6. Also the o-H₂¹³CO observations agree with those of the main iso-

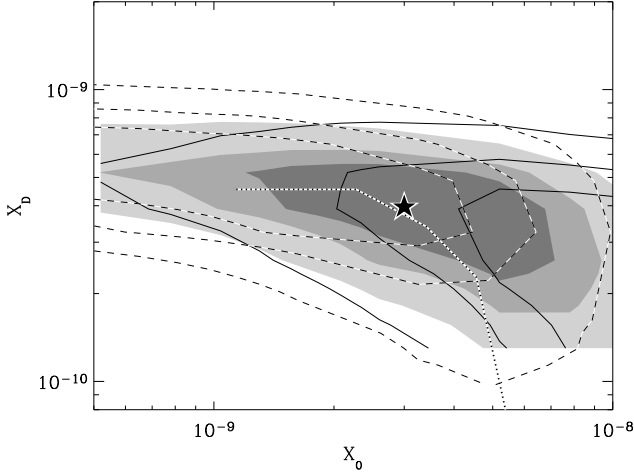


Fig. 7. Constraints on H₂CO abundances in a “drop” model for NGC 1333-IRAS4A, i.e., a model where the molecule is depleted to X_D in the regions where the density is higher than n_{de} and temperature lower than T_{ev} constrained from CO observations. The solid and dashed contours indicate the 1σ , 2σ and 4σ confidence levels for p-H₂CO and o-H₂CO, respectively whereas the grey-scale contours indicate the confidence region for the two species combined with an ortho-para ratio of 1.6. The black/white dotted line indicates the best fit relation from the o-H₂¹³CO lines. The best fit model ($X_0=3\times 10^{-9}$, $X_D=4\times 10^{-10}$) combining all lines has χ^2_{red} of 1.1 and is indicated with the “★”.

topic lines assuming a ¹²C:¹³C ratio of 70. The best fit drop model has an undepleted abundance $X_0 = 3 \times 10^{-9}$ and an abundance in the depletion region of $X_D = 4 \times 10^{-10}$. The reduced χ^2 for this model is 1.1 for 10 fitted lines (including all ortho, para and H₂¹³CO lines). This suggests that the variations in H₂CO abundances reflect, to first order, the variations due to freeze-out, with the chemical network subsequently regulating the abundances. High-resolution interferometer observations confirm this structure for IRAS 16293-2422 and L1448-C (Schöier et al., 2004).

Table 9 compares the drop abundance profiles for NGC 1333-IRAS4A with those of L1448-C and IRAS 16293-2422 (Schöier et al., 2004). Similar values for X_0 are found within a factor 3 and with the H₂CO abundance decreased by an order of magnitude in the freeze-out zone. Also the maximum constant abundance for the entire sample is in agreement with this value for X_0 , supporting the suggestion that the spread in constant H₂CO abundances reflects the size of the freeze-out zone.

A varying abundance structure is also preferred for NGC 1333-IRAS4B: as seen from Table 5 and Fig. 3, the ortho-para ratio for this particular source is less than 1. This problem is not alleviated by the introduction of a “drop” profile, which still gives an ortho-para ratio below unity and a poor fit to, in particular, the ortho-H₂CO lines. An abundance increase at low temperatures, however, does a better job: Fig. 8 shows models for NGC 1333-IRAS4B with abundance jumps

Table 9. Summary of models with varying H₂CO abundance structure.

	X_D	X_0
NGC 1333-IRAS4A	4×10^{-10}	3×10^{-9}
L1448-C ^a	1×10^{-9}	1×10^{-8}
IRAS 16293-2422 ^a	3×10^{-10}	1×10^{-8}
Sample ^b	7×10^{-11}	8×10^{-9}
NGC 1333-IRAS4B ^c	$<1\times 10^{-9}$	1×10^{-8}

^aFrom Schöier et al. (2004) fitting both single-dish and interferometer data. ^bMinimum and maximum abundances for the entire sample in this paper. ^cModel with abundance jump at 20 K. X_D for this source refer to the abundance where $T < 20$ K and X_0 to the abundance where $T > 20$ K.

at differing temperatures. An abundance jump at $T_{ev} \lesssim 30$ K from $\sim 10^{-10}$ to $\sim 10^{-8}$ makes it possible to fit the lines with an ortho-para ratio above unity, and to bring the abundance inferred from the o-H₂¹³CO lines in agreement with that of the o-H₂¹²CO lines. A jump at low temperatures also significantly improves the best fit for the two species separately. This is interesting compared with the results of Maret et al. (2004) who inferred an abundance enhancement close to 4 orders of magnitude in NGC 1333-IRAS4B, but with a rather low quality of the fit ($\chi^2_{red} \approx 7$). This suggests that the model with a jump at temperatures of 90-100 K is not adequate to describe the abundance structure for NGC 1333-IRAS4B but that other mechanisms such as the action of the protostellar outflow regulate the H₂CO abundance for this source.

To summarize these discussions: by fitting the ortho and para H₂CO lines independently for the larger sample of sources, the ortho-para ratio can be constrained statistically to be 1.6 ± 0.3 . The observed correlations with other species from the survey of Jørgensen et al. (2004c) suggest that the H₂CO abundances are related to the overall chemical network – primarily reflecting freeze-out of CO at low temperatures and high densities. This is further illustrated by fits to the NGC 1333-IRAS4A H₂CO data, which are improved with a “drop abundance” profile. In these models, the H₂CO abundance is decreased by an order of magnitude in the cold freeze-out zone. No jump in abundance in the innermost ($T \gtrsim 90$ K) region is needed, although NGC 1333-IRAS4B is best fit with an abundance increase where $T \gtrsim 20 - 30$ K. Observations of higher excitation lines are needed to constrain jumps in the hot core region. The NGC 1333-IRAS4B data suggest that for specific sources, other effects, such as the impact of the outflow, may play a role in defining the H₂CO abundance structures.

3.2. CH₃OH and CH₃CN

The upper limits for the constant CH₃OH abundances found for the sources in sample range from a few $\times 10^{-10}$ to $\sim 10^{-9}$. The upper limits are typically a factor of a few below the abundances determined from lower excitation CH₃OH lines by Buckle & Fuller (2002). However, since their abundances were calculated relative to CO, for which abundances are lower by

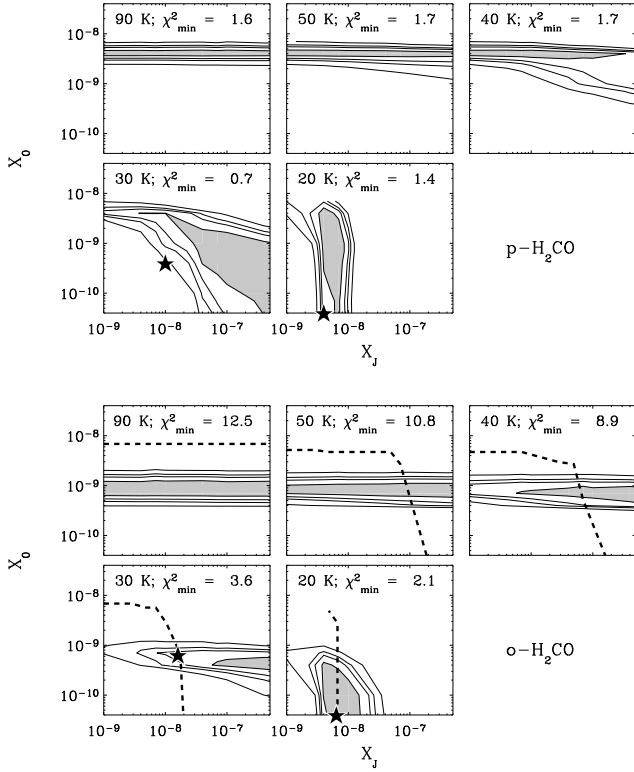


Fig. 8. χ^2 -confidence contour plots for p-H₂CO and o-H₂CO abundances (upper and lower panels, respectively) toward NGC 1333-IRAS4B. The minimum χ^2_{red} for the given jump temperature is indicated in the top of each panel. The dashed lines indicate the constraints on the abundances from the o-H₂¹³CO lines. In the $T_{\text{ev}} = 20$ K and $T_{\text{ev}} = 30$ K panels the best fit models combining the constraints for all lines (with minimum $\chi^2_{\text{red}} = 1.7$ and 3.8, respectively) have been indicated by “★”. For the other values of T_{ev} , the minimum $\chi^2_{\text{red}} > 5$.

an order of magnitude than the canonical value in the class 0 objects, the upper limits from this paper and the results of Buckle & Fuller (2002) are still consistent. Buckle & Fuller also found a slight decrease in CH₃OH abundance with bolometric temperature (i.e., lower CH₃OH abundance in the class I objects). This may again be a result of the abundance calculated relative to CO, since the CO abundance varies with envelope mass (Jørgensen et al., 2002). A similar trend was seen for the sulfur-bearing species (Buckle & Fuller, 2003, see discussion in Jørgensen et al. 2004d).

As noted by Maret et al. (2005), the CH₃OH data for NGC 1333-IRAS2 and -IRAS4B (see also Table 6) cannot be modeled with constant abundances. In the best cases such models give $\chi^2_{\text{red}} \approx 10 - 20$. NGC 1333-IRAS4A also shows mediocre fits for each of the A and E-type species with constant abundances, but still better than the two other sources ($\chi^2_{\text{red}} \approx 3 - 4$).

Our analysis uses the new collisional rate coefficients for CH₃OH recently published by Pottage et al. (2004). Compared to the old rate coefficients, the derived line intensities vary in certain cases by up to 50%. However, no systematic trends are

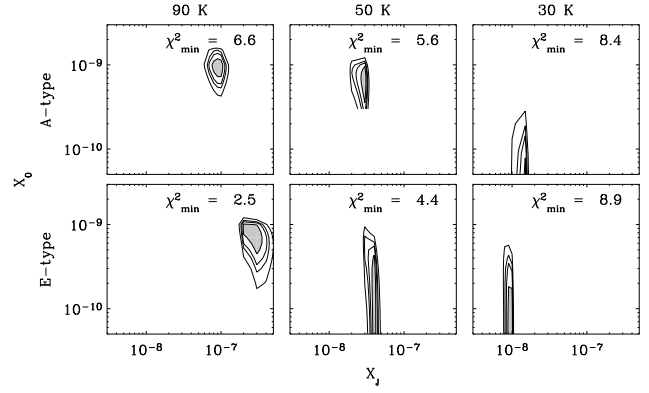


Fig. 9. χ^2 -confidence contours for jump models with varying T_{ev} for CH₃OH lines toward NGC 1333-IRAS2. The minimum χ^2_{red} is given in the upper right corner of each panel.

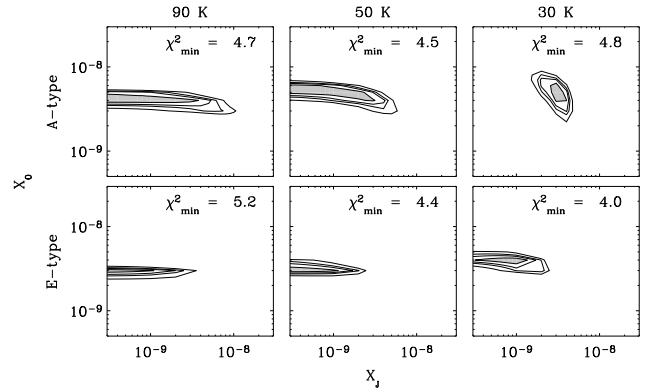


Fig. 10. As in Fig. 9 for CH₃OH lines toward NGC 1333-IRAS4A.

seen and therefore the derived abundance structures are unchanged. Still, this example illustrates that the derived abundances – especially when based on constraints from only a few lines – may be uncertain by up to a factor of 2 due to uncertainties in the collisional data alone (see also Schöier et al., 2005).

The poor fits can be improved by including evaporation of grain ice mantles at temperatures $\gtrsim 90$ K (Ceccarelli et al., 2000; Schöier et al., 2002; Maret et al., 2004, 2005). To test this, a step function for the abundance was introduced, with a jump in abundance from X_0 in the exterior to X_j in the interior at a radius corresponding to a specific temperature T_{ev} . Models were run for $T_{\text{ev}} = 30, 50$ and 90 K for each of the three NGC 1333 sources. Table 10 gives the best fit models and Fig. 9-11 show the derived χ^2 confidence plots for each of the temperatures and for each of the sources. They clearly show different behavior: NGC 1333-IRAS2 is nicely fit with a jump at 90 K, whereas NGC 1333-IRAS4B is much better fit with a jump at 30 K. For NGC 1333-IRAS4A the models suggest a best fit for a constant or “anti-jump” abundance structure.

It is also noteworthy that the best fits of both A- and E-type species are obtained for similar abundances at the best fitting evaporation temperatures. As for the H₂CO ortho-para species, no transitions between the A- and E-type CH₃OH levels are expected. The E/A-type abundance ratio, however, only

Table 10. Derived CH₃OH and CH₃CN abundances assuming abundance jumps in the inner $T > T_{ev}$ regions.

	T_{ev}	Species	X_J	X_0	χ^2_{red}
CH ₃ OH					
IRAS2	90 K	A-type (8)	9×10^{-8}	1×10^{-9}	6.6
		E-type (13)	3×10^{-7}	7×10^{-10}	2.5
IRAS4A	50 K	A-type (7)	$\leq 5 \times 10^{-9}$	4×10^{-9}	4.5 ^a
		E-type (7)	$\leq 2 \times 10^{-9}$	3×10^{-9}	4.4 ^a
IRAS4B	30 K	A-type (7)	1×10^{-7}	3×10^{-9}	2.8
		E-type (7)	9×10^{-8}	3×10^{-9}	2.7
IRAS 16293-2422 ^b	90 K	A+E-type (23)	1×10^{-7}	6×10^{-9}	1.2
CH ₃ CN					
IRAS2	90 K	A-type	7×10^{-9}	$< 3 \times 10^{-11}$	1.4

^aNo strong constraints exist on the evaporation temperature for NGC 1333-IRAS4A in accordance with the conclusion that this source is well-fitted by a constant abundance throughout the envelope (see Fig. 10). ^bResults for IRAS 16293-2422 from Schöier et al. (2002) assuming the abundances of the A- and E-type CH₃OH to be identical.

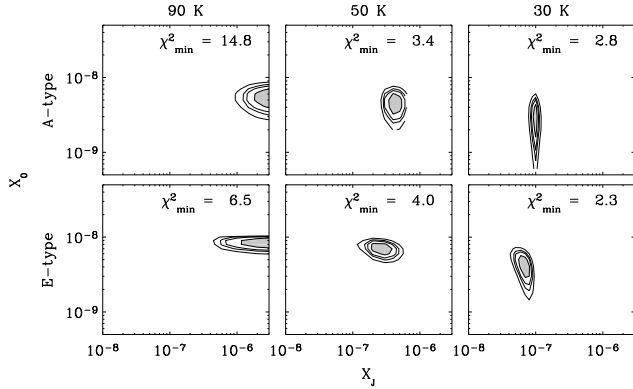


Fig. 11. As in Fig. 9 for CH₃OH lines toward NGC 1333-IRAS4B.

varies from 0.69, corresponding to thermalization at 10 K, to unity in the high temperature limit (Friberg et al., 1988). The abundances are therefore expected to be similar for the best fit models, which appears to be the case as illustrated in Fig. 9-11.

For NGC 1333-IRAS2 similar jump models were run for CH₃CN, and the best fit abundance is shown in Fig. 12. Interestingly the CH₃CN lines also give an abundance jump of approximately two orders of magnitude at 90 K, similar to what is found for the CH₃OH lines. Again jumps at lower temperatures are not favored for this source. The value of X_J for NGC 1333-IRAS2 is comparable to that derived for IRAS 16293-2422 by Schöier et al. (2002) and Cazaux et al. (2003). There is no strong evidence to suggest that the chemistry of this molecule is significantly different in the innermost envelopes around the objects discussed in this paper compared to IRAS 16293-2422.

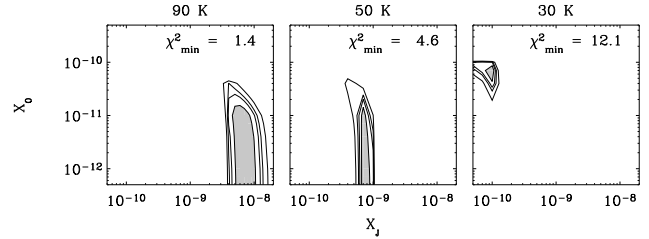


Fig. 12. χ^2 -confidence contours for jump models with varying T_{ev} for CH₃CN lines toward NGC 1333-IRAS2. The minimum χ^2_{red} is given in the upper right corner of each panel.

4. Discussion

4.1. Hot core vs. outflow

As discussed in Sect. 3.1, the H₂CO abundances are found to be consistent with constant abundances throughout the envelopes for most sources. The CH₃OH results for the three NGC 1333 sources, in contrast, imply abundance variations, but these occur over significantly different regions of the envelope. The three objects have rather similar density and temperature profiles and the observed differences therefore suggest other causes for the abundance enhancements than passive heating of the envelope material.

An important clue comes from the differing line profiles of H₂CO and CH₃OH. Fig. 13 compares the profiles for the H₂CO 5₀₅ – 4₀₄ and CH₃OH 7₋₁ – 6₋₁-E lines toward NGC 1333-IRAS2. The CH₃OH line is significantly broader, with a width of 4 km s⁻¹ compared to the 1.5 km s⁻¹ for the H₂CO line. Part of this could be due to differences in the thermal broadening if CH₃OH probes warmer gas much deeper in the envelope. The radiative transfer models, however, take this explicitly into account and it is concluded that a significantly higher turbulent broadening is required to model the observed CH₃OH lines compared with those of H₂CO and other species. This suggests

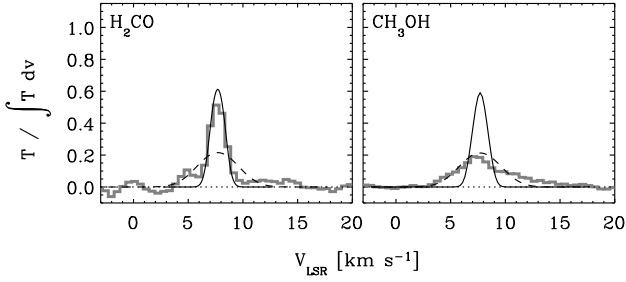


Fig. 13. Observed and modeled spectra of H₂CO 5₀₅ – 4₀₄ and CH₃OH 7₋₁6₋₁-E lines toward NGC 1333-IRAS2. The two models shown use turbulent line broadening of 0.8 km s⁻¹, which can also account for, e.g., the C¹⁸O lines modeled in Jørgensen et al. (2002) (solid line), and 2.5 km s⁻¹ (dashed line), respectively. Note how the two lines probe significantly different velocity fields in the envelope.

that the CH₃OH lines probe a different part of the envelope than H₂CO and the species discussed by Jørgensen et al. (2004c).

One explanation for the enhancements and profiles of CH₃OH could be the impact of the outflows on the inner envelopes. This was suggested to be the case for NGC 1333-IRAS4A and IRAS4B by Blake et al. (1995), who noted that the abundance enhancements can occur in the outflow shear zones probed by the very broad, kinematically distinct CS and CH₃OH lines. Large enhancements of CH₃OH are seen in the shocks driven by the outflows from a number of protostellar sources where the shock is well separated from the central protostar including L1448-C, L1157 and NGC 1333-IRAS2 (e.g., Bachiller et al., 1995; Bachiller & Pérez Gutiérrez, 1997; Jørgensen et al., 2004a). CH₃OH is one of the molecules that shows the largest jumps in abundances between cold and warm gas and therefore traces more clearly the origin of the abundance enhancements.

An outflow scenario could explain the relatively low desorption temperature found for the CH₃OH lines as well as the fits to the H₂CO lines for NGC 1333-IRAS4B discussed in Sect. 3.1.3. If these species are desorbed from grains due to the action of the outflow, they could thermalize at temperatures closer to that of the envelope, i.e., lower than in the small “hot core” region. NGC 1333-IRAS4A is remarkable since the fits to the CH₃OH lines do not require a jump in abundance. This difference from NGC 1333-IRAS4B could be caused by the differences in the outflow morphologies: Di Francesco et al. (2001) imaged the NGC 1333-IRAS4 region at high resolution and found that the outflows are probed by the wings of H₂CO and CS. The images show that the IRAS4B outflow is more compact with emission over a $\approx 15''$ region comparable to the 350 GHz JCMT single-dish beam. The morphology thus suggests that enhancements for the NGC 1333-IRAS4B outflow occur on scales where the single-dish observations are the most sensitive. Also the SiO $J = 5-4$ line at 217.1 GHz is only detected toward NGC 1333-IRAS4A and not IRAS4B. This indicates that the CH₃OH enhancements in IRAS4B are not directly associated with a high velocity shock but more likely result from the shear between the envelope

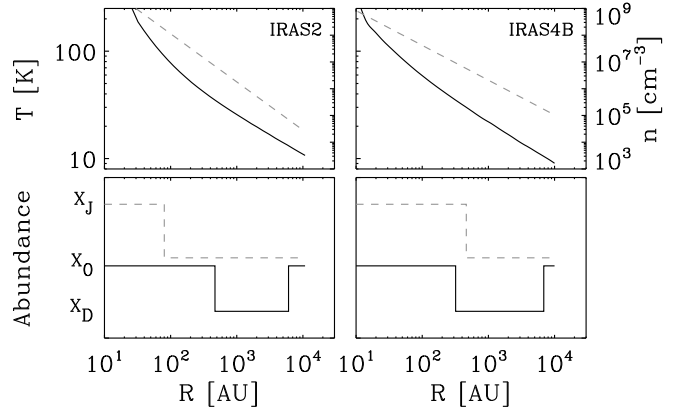


Fig. 14. Comparison of the inferred temperature, density and abundance structures in NGC 1333-IRAS2 (left) and NGC 1333-IRAS4B (right). The upper panels show the temperature (black solid line) and density (grey dashed line) profiles for each source. The lower panels show the inferred CO drop abundance (black solid line) and CH₃OH jump abundance (grey dashed line) profiles (Jørgensen et al., 2005, this paper).

and outflow. Note also that direct images of outflow induced shocks (Bachiller & Pérez Gutiérrez, 1997; Garay et al., 2000; Bachiller et al., 2001; Jørgensen et al., 2004a) indicate that CH₃OH does not survive at the highest shock speeds, which could further explain the differences between IRAS4A and IRAS4B. In contrast, the impact of the outflow in NGC 1333-IRAS2 is on much smaller scales, more heavily diluted in the single-dish beam. Fig. 14 compares the inferred abundance structures for NGC 1333-IRAS2 and -IRAS4B.

4.2. CS $J = 10 - 9$ and HDO as dense gas probes

Further support for the importance of the outflows comes from observations of high excitation CS $J = 10 - 9$ and HDO lines obtained with the JCMT. For CS $J = 10 - 9$, broad lines (FWHM ≈ 8 km s⁻¹) are detected toward both NGC 1333-IRAS4A and IRAS4B (Fig. 15), which lack the central narrow peak seen for the lower excitation lines (Fig. 16). Although, the absolute calibration may be somewhat uncertain, the CS $J = 10 - 9$ line is approximately 5 times stronger toward IRAS4B than IRAS4A, consistent with the above conclusion that the dense outflow gas fills a larger fraction of the beam for IRAS4B. This is in contrast to the lower excitation CS lines reported, e.g., by Blake et al. (1995) and Jørgensen et al. (2004c), which support a more compact origin of the CS outflow emission in IRAS4B than IRAS4A.

Table 11 compares the predictions for the CS $J = 10 - 9$ line intensity assuming CS abundances in the quiescent envelope from the models of Jørgensen et al. (2004c). The envelope models predict significantly less emission than observed for IRAS4A and IRAS4B, but the non-detection toward IRAS2 is consistent within the 3σ noise level. Note that the CS intensities in Jørgensen et al. (2004c) were found by integration over

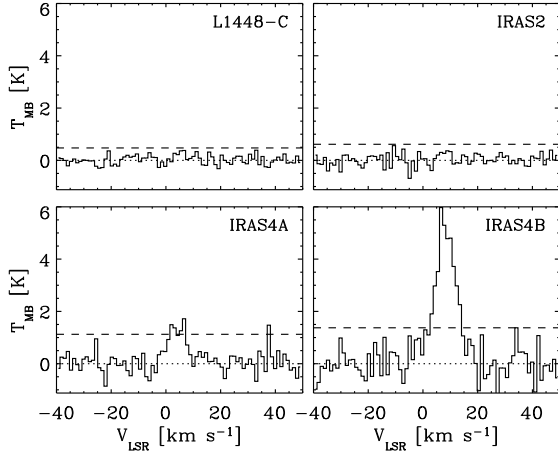


Fig. 15. CS $J = 10 - 9$ observations of L1448-C and the three NGC 1333 sources. In each plot the dashed line indicates the 3σ detection limit. Lower 6 panels: Comparison between CS lines probing different excitation conditions in the envelopes, i.e., depths of NGC 1333-IRAS2 and -IRAS4B. The lowest excitation 3–2 lines are from IRAM 30 m observations the remainder from JCMT observations.

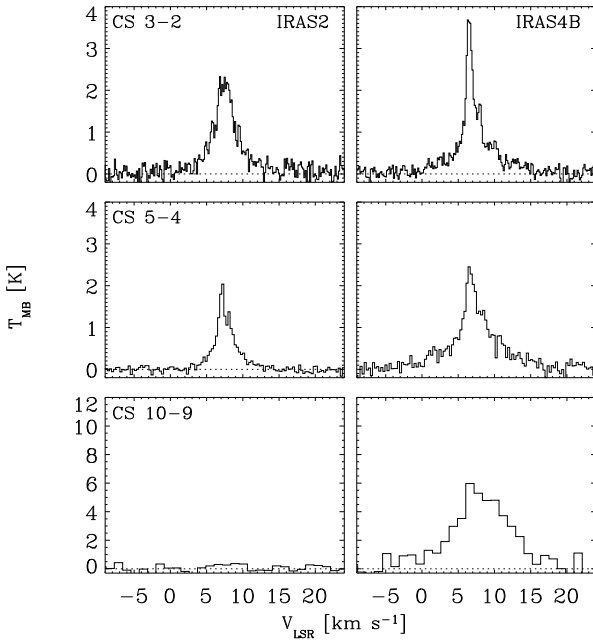


Fig. 16. Comparison between CS lines probing different excitation conditions in the envelopes, i.e., depths of NGC 1333-IRAS2 and -IRAS4B. The lowest excitation 3–2 lines are from IRAM 30 m observations the remainder from JCMT observations.

$\pm 2 \text{ km s}^{-1}$ from the systemic velocity: for the CS $J = 10 - 9$ lines the emission integrated over this velocity range only contributes 20–25% of the total integrated emission and is still underestimated by the envelope models, especially for IRAS4B. Again this suggests that the observed CS $J = 10 - 9$ emission

Table 11. Observed and predicted line intensities ($\int T_{\text{MB}} d\nu$) for CS $J = 10 - 9$ for the three sources in NGC 1333.

Source	$I_{\text{mod}} [\text{K km s}^{-1}]^a$	$I_{\text{obs}} [\text{K km s}^{-1}]^b$
IRAS2	1.8	< 2
IRAS4A	1.7	12 (3)
IRAS4B	1.1	51 (11)

^aPredicted CS $J = 10 - 9$ line intensity adopting best fit abundances for each source from Jørgensen et al. (2004c). ^bTotal line emission from Gaussian fits (IRAS4A and IRAS4B) or as 3σ upper limit (IRAS2). For IRAS4A and IRAS4B the number in parenthesis indicate the line emission integrated over $\pm 2 \text{ km s}^{-1}$ from the systemic velocity.

probes different material than traced in the bulk envelope material.

Another simple estimate can be made assuming that the CS emission comes from a medium with a constant density and kinetic temperature. Using a non-LTE escape probability code, *Radex* (Jansen et al., 1994; Schöier et al., 2005), the CS column density is estimated adopting a density of $3 \times 10^6 \text{ cm}^{-3}$ and kinetic temperature of 100 K (Blake et al., 1995), consistent with the intensity of the wing emission from the CS 5–4 and 7–6 lines from Jørgensen et al. (2004c). A high column density of $\sim 5 \times 10^{14} \text{ cm}^{-2}$ is needed to produce the observed CS 10–9 emission. Even at such high column densities, the emission is found to be optically thin. This column density is an order of magnitude larger than found from the lower excitation lines by Blake et al. (1995) and corresponds to $\approx 5 - 10\%$ of the estimated CO abundance in the outflowing material based on the CO column density calculated by Blake et al..

In contrast to the CS $J = 10 - 9$ lines, HDO $2_{11} - 2_{12}$ is detected only toward NGC 1333-IRAS2 and not IRAS4A and IRAS4B (see Fig. 17). Like CS 10–9 this line probes the warm, dense gas with an upper level energy of 90 K. The observed line is narrow (FWHM of $\approx 2.5 \text{ km s}^{-1}$) compared to the $\approx 8 \text{ km s}^{-1}$ for the CS $J = 10 - 9$ and $\approx 4 \text{ km s}^{-1}$ for the CH₃OH lines toward IRAS4A and IRAS4B. This suggests that this line has its origin in a “hot inner region” of the NGC 1333-IRAS2 envelope, although relation to the small-scale outflow (as seen in high resolution maps by Jørgensen et al., 2004b) cannot be ruled out. Enhancements of HDO by up to a factor of 10 were derived for the IRAS 16293-2422 outflow by Stark et al. (2004), but Parise et al. (2005) show that observations of a larger number of HDO transitions are better explained by an abundance enhancement by two orders of magnitude in the innermost quiescent envelope. Observations of more transitions will be needed before either scenario can be confirmed or ruled out for NGC 1333-IRAS2. Since both CH₃OH and CH₃CN observations indicate the presence of warm gas with abundance jumps in the inner ($T < 90 \text{ K}$) region, NGC 1333-IRAS2 still seems the best candidate for further comparative studies of the passively heated, hot inner regions of low-mass protostellar envelopes.

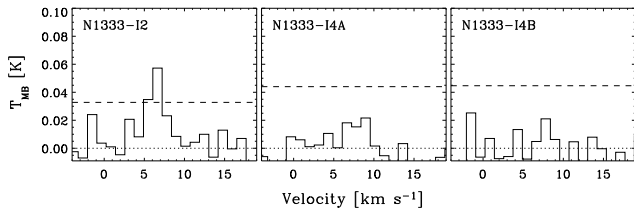


Fig. 17. Observations of the HDO $2_{11} - 2_{12}$ line at 241.5616 GHz toward the three NGC 1333 sources observed in the CH₃OH 5–4 setting. HDO is only detected toward NGC 1333-IRAS2. In each plot the dashed line indicates the 3σ detection limit.

4.3. Comparison with IRAS 16293-2422

The above results again raise the question what causes the richness of lines in IRAS 16293-2422 (even taking into its smaller distance and higher luminosity compared to, e.g., the NGC 1333 sources) since its abundances in the outer envelope are comparable to those of other sources. One explanation may be that its small-scale physical structure is significantly different from that of the remaining sources. The central binary system has a separation of 8–10'' and affects the material in the envelope with emission from the various species centered around one or both components (Mundy et al., 1992; Schöier et al., 2004). Furthermore the circumbinary envelope appears to have an inner cavity of size comparable to the binary separation. It may be that this relatively wide (~ 1000 AU) binary pushes material to larger distances where it can more easily be observed through single-dish observations with ~ 10 – $15''$ beams. Alternatively, the circumbinary envelope may be heated on larger scales through each of the relatively luminous components compared with that expected from a single component in a simple spherical envelope. Finally, interferometer maps also show velocity gradients indicating that the outflow affects the envelope material close to the central protostar. It is possible that the outflow processing leads to abundance enhancements of the organic species on larger scales than the passively heated hot core, thus providing a larger filling factor of the single-dish beam.

5. Conclusions

We have presented an analysis of H₂CO and CH₃OH line observations for a sample of 18 pre- and protostellar cores which have previously been studied through continuum and line observations and detailed radiative transfer modeling (Jørgensen et al., 2002, 2004c). These results complement the results by Maret et al. (2004, 2005) for a subset of sources. In addition, observations and limits for high excitation CS $J = 10 - 9$ transitions and lines of HDO and CH₃CN are presented for a subset of sources. Molecular abundances are derived through Monte Carlo line radiative transfer and compared to the results from the survey of Jørgensen et al. (2004c). The main conclusions are:

- The H₂CO data of most sources can be well-fitted by constant abundances throughout their envelopes with an ortho-

para ratio of 1.6 ± 0.3 . This implies thermalization of H₂CO at low temperatures, e.g., on grain ice-mantles. Higher angular resolution data are needed to constrain the presence of any abundance jumps in the inner warm envelopes.

- The H₂CO abundances are related to the chemical network of the other species indicating that the same processes regulate their abundances. As an example the H₂CO data for NGC 1333-IRAS4A are well-fit by “drop abundance” profiles with a decrease in abundance from a few $\times 10^{-9} - 10^{-8}$ to a few $\times 10^{-10}$ in a limited part of the envelope, bounded inwards by the desorption temperature and outwards by a density corresponding to the lifetime of the core. A counter example is provided by NGC 1333-IRAS4B, where an abundance increase is only needed where the temperature rises above 20–30 K with no enhancement in the outermost regions. This indicates that for some sources other effects, such as the impact of an outflow, may be important for regulating the H₂CO abundances.
- The upper limits to the CH₃OH abundances for the entire sample are a few $\times 10^{-10} - 10^{-9}$. These results are consistent with the abundances determined by Buckle & Fuller (2002) from lower excitation lines.
- CH₃OH observations for NGC 1333-IRAS2 and NGC 1333-IRAS4B require abundance jumps of at least two orders of magnitude at 90 K and 30 K, respectively. Together with the significantly broader lines of CH₃OH compared with H₂CO and other species, this suggests that the abundance increase for IRAS4B, in particular, is due to a compact outflow interacting with the nearby envelope. This is further supported by the broad high frequency CS $J = 10 - 9$ line, detected very strongly toward this source. HDO and CH₃CN, in contrast, are only observed for NGC 1333-IRAS2 - possibly reflecting the presence of a passively heated, warm inner region for this source where molecules can evaporate. The CH₃CN data for NGC 1333-IRAS2 also require a jump in abundance at 90 K by about two orders of magnitude.

This paper reinforces the importance of identifying (if possible) unique chemical tracers of material heated “passively” by a central protostar and by shocked material in outflows. Even relatively high excitation lines from single-dish observations (such as the CS $J = 10 - 9$ lines) may be affected by the outflow and can provide a good indication of the filling factor of dense shocked material. Future Herschel-HIFI observations may provide additional tests of the chemical structure by observations of high frequency lines, but the fact that shock and envelope chemistry are spatially unresolved may be problematic for these large beam data. Possibly the best way of distinguishing the different chemical scenarios will be through high angular resolution, high excitation observations with facilities such as the SMA and ALMA - or from studies of outflows well-separated from the central protostar as, for example, done in Bachiller & Pérez Gutiérrez (1997) and Jørgensen et al. (2004a). Better knowledge about the physical properties of the inner envelopes will also be important, since the adopted envelope models are extrapolations from the larger-scale observations of the cold dust in the outer enve-

lope. Infrared observations with the Spitzer Space Telescope can place better constraints there.

Acknowledgements. The authors thank Sebastien Maret and Cecilia Ceccarelli for interesting discussions and communicating their results prior to publication. The referee is thanked for detailed comments that helped clarifying the paper. The research of JKJ is funded by a NOVA network 2 Ph.D. stipend. FLS acknowledges support from the Swedish Research Council. Astrochemistry research in Leiden is supported by an NWO Spinoza grant.

References

- Bachiller, R., Liechti, S., Walmsley, C. M., & Colomer, F. 1995, *A&A*, 295, L51
- Bachiller, R., Pérez Gutiérrez, M., Kumar, M. S. N., & Tafalla, M. 2001, *A&A*, 372, 899
- Bachiller, R. & Pérez Gutiérrez, M. 1997, *ApJ*, 487, L93
- Bacmann, A., Lefloch, B., Ceccarelli, C., et al. 2003, *ApJ*, 585, L55
- Blake, G. A., Sandell, G., van Dishoeck, E. F., et al. 1995, *ApJ*, 441, 689
- Blake, G. A., van Dishoeck, E. F., Jansen, D. J., Groesbeck, T. D., & Mundy, L. G. 1994, *ApJ*, 428, 680
- Bottinelli, S., Ceccarelli, C., Lefloch, B., et al. 2004, *ApJ*, 615, 354
- Buckle, J. V. & Fuller, G. A. 2002, *A&A*, 381, 77
- . 2003, *A&A*, 399, 567
- Cazaux, S., Tielens, A. G. G. M., Ceccarelli, C., et al. 2003, *ApJ*, 593, L51
- Ceccarelli, C., Castets, A., Caux, E., et al. 2000, *A&A*, 355, 1129
- Ceccarelli, C., Castets, A., Loinard, L., Caux, E., & Tielens, A. G. G. M. 1998, *A&A*, 338, L43
- Di Francesco, J., Myers, P. C., Wilner, D. J., Ohashi, N., & Mardones, D. 2001, *ApJ*, 562, 770
- Friberg, P., Hjalmarsen, A., Madden, S. C., & Irvine, W. M. 1988, *A&A*, 195, 281
- Garay, G., Mardones, D., & Rodríguez, L. F. 2000, *ApJ*, 545, 861
- Jansen, D. J., van Dishoeck, E. F., & Black, J. H. 1994, *A&A*, 282, 605
- Jørgensen, J. K., Hogerheijde, M. R., Blake, G. A., et al. 2004a, *A&A*, 415, 1021
- Jørgensen, J. K., Hogerheijde, M. R., van Dishoeck, E. F., Blake, G. A., & Schöier, F. L. 2004b, *A&A*, 413, 993
- Jørgensen, J. K., Schöier, F. L., & van Dishoeck, E. F. 2002, *A&A*, 389, 908
- Jørgensen, J. K., Schöier, F. L., & van Dishoeck, E. F. 2004c, *A&A*, 416, 603
- . 2005, *A&A*, in press. (astro-ph/0501623)
- Kahane, C., Lucas, R., Frerking, M. A., Langer, W. D., & Encrenaz, P. 1984, *A&A*, 137, 211
- Mangum, J. G. & Wootten, A. 1993, *ApJS*, 89, 123
- Maret, S., Ceccarelli, C., Caux, E., et al. 2004, *A&A*, 416, 577
- Maret, S., Ceccarelli, C., Tielens, A. G. G. M., et al. 2005, *A&A*, in prep.
- Mundy, L. G., Wootten, A., Wilking, B. A., Blake, G. A., & Sargent, A. I. 1992, *ApJ*, 385, 306
- Parise, B., Caux, E., Castets, A., et al. 2005, *A&A*, 431, 547
- Pottage, J. T., Flower, D. R., & Davis, S. L. 2004, *MNRAS*, 352, 39
- Schöier, F. L., Jørgensen, J. K., van Dishoeck, E. F., & Blake, G. A. 2002, *A&A*, 390, 1001
- . 2004, *A&A*, 418, 185
- Schöier, F. L., van der Tak, F. F. S., van Dishoeck, E. F., & Black, J. H. 2005, *A&A*, 432, 369
- Shu, F. H. 1977, *ApJ*, 214, 488
- Stark, R., Sandell, G., Beck, S. C., et al. 2004, *ApJ*, 608, 341
- van Dishoeck, E. F., Blake, G. A., Jansen, D. J., & Groesbeck, T. D. 1995, *ApJ*, 447, 760
- van Zadelhoff, G.-J., Dullemond, C. P., van der Tak, F. F. S., et al. 2002, *A&A*, 395, 373

Appendix A: Line widths from gaussian fits

Table A.1–A.2 lists the line widths (FWHM) for the observations where Gaussians could be fitted. For the lower excitation H₂CO observations not listed here the lines were integrated over ± 2 km s⁻¹.

Table A.1. Line widths (FWHM in km s⁻¹) for H₂CO lines (see also Maret et al. (2004)).

Source	$\Delta v(5_{05} - 4_{04})$	$\Delta v(5_{15} - 4_{14})$
L1448-I2	1.5	0.96
L1448-C	1.1	^b
N1333-I2	1.9 ^a	^b
N1333-I4A	3.5 ^a	4.1 ^a
N1333-I4B	3.1 ^a	4.0 ^a
L1527	1.0	0.9
VLA1623	0.63	^b
L483	0.93	1.4
L723	1.6	2.3
L1157	0.52	1.1
CB244	1.4	1.8
L1551	1.6	1.3
L1489	...	2.0 ^a
TMR1	...	1.9

Notes: ^aNon-Gaussian line profile. Intensity in Table 1 refers to line integrated over ± 2 km s⁻¹. Line width defined as $\Delta v = \int T dv / (1.064 T_{\text{peak}})$ where the integral is over the total line profile and T_{peak} is the temperature at the line peak. ^bInsufficient spectral resolution to estimate width.

Table A.2. CH₃OH line widths (FWHM in km s⁻¹) for sources in NGC 1333.

Line	Frequency	IRAS2	IRAS4A	IRAS4B
5 _K - 4 _K band; E-type				
+0E	241.7002	3.5	6.0 ^a	3.4 ^a
-1E	.7672	3.0 ^a	6.2 ^a	3.4 ^a
-4E	.8132	4.9
+4E	.8296	2.1
+3E	.8430	–	–	– †
-3E	.8523	3.9
+1E	.8790	3.4	6.0	3.4
±2E	.9044	3.4	6.9	3.5
5 _K - 4 _K band; A-type				
+0A	241.7914	2.6 ^a	5.7 ^a	3.2 ^a
±4A	.8065	3.2
±3A	.8329	3.4	6.0	2.8
-2A	.8430	–	–	– †
+2A	.8877	3.2	6.0	4.3
7 _K - 6 _K band; E-type				
-1E	338.3446	4.5 ^a	7.7 ^a	4.4 ^a
-4E	.5040	3.3
+4E	.5302	3.2
-3E	.5599	3.0
+3E	.5831	3.1	5.3	3.3
+1E	.6150	3.3 ^a	7.0	4.4
7 _K - 6 _K band; A-type				
+0A	338.4086	4.8 ^a	7.5 ^a	4.4 ^a
±4A/-2A	.5127	3.3	7.7	5.4
±3A	.5419	4.6	7.7	5.6
+2A	.6399	3.0	7.8	4.3

“†”The 5 - 4 +3E and -2A lines are blended at 241.8430 GHz.

^aLines asymmetric. No Gaussian fitted. Line width defined as $\Delta v = \int T dv / (1.064 T_{\text{peak}})$ where the integral is over the total line profile and T_{peak} is the temperature at the line peak.